PHYSICAL REVIEW B **96**, 235137 (2017)

Structural, electronic, and thermodynamic properties of curium dioxide: Density functional theory calculations

Ling Hou,[1,2,3] Wei-Dong Li,[1] Fangwei Wang,[3,4] Olle Eriksson,[5] and Bao-Tian Wang[2,3,*]
[1]*Institute of Theoretical Physics and Department of Physics, Shanxi University, Taiyuan 030006, China*
[2]*Institute of High Energy Physics, Chinese Academy of Sciences (CAS), Beijing 100049, China*
[3]*Dongguan Neutron Science Center, Dongguan 523803, China*
[4]*Beijing National Laboratory for Condensed Matter Physics, Institute of Physics, Chinese Academy of Sciences, Beijing 100080, China*
[5]*Department of Physics and Astronomy, Division of Materials Theory, Uppsala University, Box 516, SE-75120 Uppsala, Sweden*

(Received 9 September 2017; revised manuscript received 12 December 2017; published 22 December 2017)

We present a systematic investigation of the structural, magnetic, electronic, mechanical, and thermodynamic properties of CmO_2 with the local density approximation (LDA)+U and the generalized gradient approximation (GGA)+U approaches. The strong Coulomb repulsion and the spin-orbit coupling (SOC) effects on the lattice structures, electronic density of states, and band gaps are carefully studied, and compared with other AO_2 (A = U, Np, Pu, and Am). The ferromagnetic configuration with half-metallic character is predicted to be energetically stable while a charge-transfer semiconductor is predicted for the antiferromagnetic configuration. The elastic constants and phonon spectra show that the fluorite structure is mechanically and dynamically stable. Based on the first-principles phonon density of states, the lattice vibrational energy is calculated using the quasiharmonic approximation. Then, the Gibbs free energy, thermal expansion coefficient, specific heat, and entropy are obtained and compared with experimental data. The mode Grüneisen parameters are presented to analyze the anharmonic properties. The Slack relation is applied to obtain the lattice thermal conductivity in temperature range of 300–1600 K. The phonon group velocities are also calculated to investigate the heat transfer. For all these properties, if available, we compare the results of CmO_2 with other AO_2.

DOI: 10.1103/PhysRevB.96.235137

I. INTRODUCTION

Actinides and their compounds play an important role in the nuclear fuel cycle and exhibit many interesting physical characters due to their half-filled $5f$ orbitals [1–5]. In any methodological framework, $5f$ actinide compounds are extremely challenging due to the interplay of various energy scales determined by electronic correlations on the f states, spin-orbit coupling (SOC), and crystal field effects and have attracted much attention [4–15]. Without including the on-site Coulomb repulsion, the pure density functional theory (DFT) method would result in an error conducting ground state for many actinide dioxides [4–6,8,16,17]. The insulator nature for these correlated electronic systems can be well reproduced using the DFT+U [17,18], the hybrid density functional HSE (Heyd, Scuseria, and Enzerhof) [4,5,8], the self-interaction corrected local spin-density (SIC-LSD) approximation [6], and local density approximation (LDA) plus dynamical mean-field theory [7] calculations. The DFT+U calculations also reported better results of phonon spectra and phonon density of states (PhDOS) than the pure DFT for PuO_2 [19] and UO_2 [20], as examined by recent experiments [9,12,21]. The effects of SOC and crystal field are found to be critically important in obtaining the ground-state magnetic structures for some actinides [22–24]. In our previous study of PuH_2 and PuH_3 [22], we found that reasonable phonon spectra can only be obtained by considering both the Coulomb repulsion and SOC simultaneously. The richness of these $5f$-multiorbital electronic properties in actinides supplies a treasure trove to investigate.

Among actinide oxides, the dioxides are the most stable and the most relevant members in the nuclear fuel cycle [6]. Among the actinide dioxide series from Th (f^0) to Fm (f^{10}), PuO_2 and AmO_2 are at the intermediate zone and their $5f$ orbitals have the largest overlap with oxygen $2p$ orbitals, in the compounds before PuO_2 (ThO_2–NpO_2), the $5f$ orbitals appear to exhibit localized behavior above the O $2p$ orbitals, while after AmO_2 (CmO_2–FmO_2), the $5f$ orbitals appear as localized states below the O $2p$ orbital.

In our previous studies, we have systematically investigated the ground-state properties (and high-pressure features) of ThO_2 [25], NpO_2 [17], PuO_2 [19], AmO_2 [26], and UO_2 [20]. While NpO_2 and UO_2 are predicted to be Mott insulators, PuO_2 and AmO_2 are found to be charge-transfer insulators. Along with increasing Z, the ionicity decreases from ThO_2 to AmO_2 [19,26]. In the present work, we would like to extend our investigation to CmO_2, which has not been studied a lot in experiments [27–30] and in theoretical calculations [5,6,31–37]. We will utilize the LDA+U and the generalized gradient approximation (GGA)+U schemes due to Dudarev *et al.* [18] to calculate the lattice parameters, magnetic states, electronic structure, mechanical features, phonon dispersions, and thermodynamic properties of CmO_2. We will discuss how the choice of U as well as the relativistic effects in terms of the SOC affect those properties. The nature of the chemical bonding of Cm-O will be presented, both qualitatively and quantitatively. Various thermodynamic properties that are important for CmO_2 in the fuel cycle will be presented in a wide temperature range.

The present paper is organized as follows. In the following section, we present our calculation methodology and the theoretical formalism. In Sec. III, we give the results of structure, magnetic states, electronic structure, elasticity,

---

[*] Author to whom correspondence should be addressed: wangbt@ihep.ac.cn

2469-9950/2017/96(23)/235137(13)

chemical-bonding characters, phonon dispersions, and various thermodynamic properties. In Sec. IV, we present a summarizing discussion of the results. Then, we summarize the main conclusions of this work in Sec. V.

II. COMPUTATIONAL METHODS

A. Computational details

The calculations are performed at the DFT level, employing the projector augmented wave method as implemented in the VASP package [38]. The LDA and the Perdew, Burke, and Ernzerhof (PBE) form of the GGA [39,40] are chosen to describe the exchange-correlation energy. A cutoff energy of 950 eV is used for the set of plane waves. The k-point meshes in the full wedge of the Brillouin zone (BZ) are sampled by $8 \times 8 \times 8$ Monkhorst-Pack [41] grids. The curium $6s^2 7s^2 6p^6 6d^2 5f^6$ and oxygen $2s^2 2p^4$ electrons are treated as valence electrons. The strong on-site Coulomb repulsion among the localized Cm 5f electrons is described by using the LDA/GGA+U formulated by Dudarev *et al.* [18,42,43], where the double counting correction has been included as in the fully localized limit [44]. In this scheme, the total LDA (GGA) energy functional is of the form

$$E_{\mathrm{LDA(GGA)+U}} = E_{\mathrm{LDA(GGA)}} + \frac{U-J}{2} \sum_{\sigma} [\mathrm{Tr}\rho^{\sigma} - \mathrm{Tr}(\rho^{\sigma}\rho^{\sigma})], \quad (1)$$

where ρ^{σ} is the density matrix of f states with spin σ, while U and J are the spherically averaged screened Coulomb energy and the exchange energy, respectively. In our study, the Coulomb U is treated as a variable, while the parameter J is fixed to be $J = 0.5$ eV. Due to the fact that only the difference between U and J is significant in Dudarev's approach [18], for simplicity, we label them as one single parameter, named U. In some cases of our calculations, the full relativistic effects are included in terms of the SOC. Comparing with the scheme through the solution of Dirac equation for SOC, the perturbative treatment of SOC implemented in VASP is also a good approximation for actinides [20,45]. The theoretical equilibrium volume V, bulk modulus B, and pressure derivative of the bulk modulus B' are obtained by fitting the energy-volume data in the third-order Birch-Murnaghan equation of state (EOS) [46].

B. Elastic properties and Debye temperature

Based on the Hooke's law, the elastic constants C_{11}, C_{12}, and C_{44} are calculated by applying stress tensors with various small strains onto the equilibrium structures. The strain amplitude δ is varied in steps of 0.006 from $\delta = -0.036$ to 0.036. A detailed calculation method can be found in Refs. [19,47]. After having obtained the elastic constants, the polycrystalline bulk modulus B and shear modulus G are calculated from the Voigt-Reuss-Hill (VRH) approximations [48] through $B = \frac{1}{2}(B_V + B_R)$ and $G = \frac{1}{2}(G_V + G_R)$. The Young's modulus E and Poisson's ratio ν are calculated through $E = 9BG/(3B + G)$ and $\nu = (3B - 2G)/[2(3B + G)]$. The Debye temperature θ_D can be determined from the elastic constants within the Debye theory, in which the vibrations of the solid are considered as elastic waves, and the Debye temperature of the solid is related to an averaged sound velocity [49], which is calculated by

$$\theta_D = \frac{h}{k_B}\left(\frac{3n}{4\pi\Omega}\right)^{1/3} \upsilon_m, \quad (2)$$

where h and k_B are Planck and Boltzmann constants, respectively, n is the number of atoms in the molecule, Ω is molecular volume, and υ_m is the average sound wave velocity. Approximately, υ_m can be given by

$$\upsilon_m = \left[\frac{1}{3}\left(\frac{2}{\upsilon_t^3} + \frac{1}{\upsilon_l^3}\right)\right]^{-1/3}, \quad (3)$$

where $\upsilon_t = \sqrt{G/\rho}$ (ρ is the density) is the transverse elastic wave velocity and $\upsilon_l = \sqrt{(3B + 4G)/3\rho}$ is the longitudinal elastic wave velocity.

C. Phonon dispersion and thermodynamic properties

We use the direct method as implemented in the YPHON code [50] to calculate the phonon curves in the BZ and the corresponding phonon density of states (PhDOS). In calculating the force constants, a $2 \times 2 \times 2$ supercell of the primitive cell is sampled with a $6 \times 6 \times 6$ k points.

Based on our calculated total energy and PhDOS, we can further calculate the thermodynamic properties using the quasiharmonic approximation (QHA) [20,51]. Under the QHA, the Gibbs free energy $G(T,P)$ at temperature (T) and pressure (P) can be written as $G(T,P) = F(T,V) + PV$. The Helmholtz free energy $F(T,V)$ at T and volume (V) is defined as

$$F(T,V) = E(V) + F_{\mathrm{vib}}(T,V) + F_{\mathrm{el}}(T,V), \quad (4)$$

where $E(V)$ is the ground-state total energy, $F_{\mathrm{vib}}(T,V)$ is the vibrational energy of the lattice ions and $F_{\mathrm{el}}(T,V)$ is the thermal electronic contribution. $F_{\mathrm{vib}}(T,V)$ can be calculated by

$$F_{\mathrm{vib}}(T,V) = k_B T \int_0^{\infty} g(\omega) \ln\left[2\sinh\left(\frac{\hbar\omega}{2k_B T}\right)\right] d\omega, \quad (5)$$

where ω represents the phonon frequencies and $g(\omega)$ is the PhDOS. F_{el} can be calculated by [52,53]

$$F_{\mathrm{el}}(T,V) = E_{\mathrm{el}} - TS_{\mathrm{el}} = -\frac{(\pi k_B)^2}{6} D(\epsilon_F) T^2, \quad (6)$$

where E_{el} is the internal electronic energy [54] written as $E_{\mathrm{el}} = \frac{(\pi k_B)^2}{6} D(\epsilon_F) T^2$, S_{el} is the electronic contribution to the entropy written as $S_{\mathrm{el}} = \int_0^T \frac{1}{T'}(\frac{\partial E}{\partial T'})_V dT' = 2\frac{E_{\mathrm{el}}}{T}$, and $D(\epsilon_F)$ is the electronic density of states at the Fermi level.

The specific heat at constant volume C_V can be calculated by [19]

$$C_V = k_B \int_0^{\infty} g(\omega) \left(\frac{\hbar\omega}{k_B T}\right)^2 \frac{\exp\frac{\hbar\omega}{k_B T}}{\left(\exp\frac{\hbar\omega}{k_B T} - 1\right)^2} d\omega, \quad (7)$$

while the specific heat at constant pressure C_P can be obtained through the thermodynamic relationship $C_P - C_V = \alpha_V^2(T)B(T)V(T)T$, where the thermal-expansion coefficient $\alpha_V(T)$ is written as $\alpha_V(T) = \frac{1}{V}(\frac{\partial V}{\partial T})_P$.

For the fluorite-type curium dioxide, the efficient heat carriers were to be their acoustic branches [55]. For temperature $T \geqslant \theta_D$, we predict the lattice thermal conductivity k_L here by the Slack theory [56,57]

$$k_L = A\frac{\bar{M}\theta_D^3(T)\delta(T)n^{1/3}}{\gamma^2(T)T}, \tag{8}$$

where A is a physical constant with the value of 3.1×10^{-6}, $\bar{M}$ is the average mass per atom in the crystal, θ_D is the Debye temperature, δ is the cube root of the average volume per atom, n is the number of atoms in the primitive unit cell, and $\gamma(T)$ is the Grüneisen parameter. The units of k_L and δ in Eq. (8) are W m^{-1} k^{-1} and Å, respectively. With reasonable expressions for the Debye temperature and acoustic Grüneisen parameter to describe the harmonic phonon branches and the anharmonic interactions between different phonon branches, Eq. (8) can provide accurate predictions for a material's thermal conductivity.

Within the isotropic approximation, $\theta_D(T)$ can be calculated by [58]

$$\theta_D(T) = \frac{\hbar}{k_B}[6\pi^2 V^{1/2}(T)n]^{1/3} f(\nu)\sqrt{\frac{B(T)}{M}}, \tag{9}$$

where $B(T)$ is the bulk modulus, M is the molecular mass per formula unit, ν stands for the material's Poisson ratio, and $f(\nu)$ can be expressed as

$$f(\nu) = 3^{1/3}\left[2\left(\frac{2}{3}\frac{1+\nu}{1-2\nu}\right)^{3/2} + \left(\frac{1}{3}\frac{1+\nu}{1-\nu}\right)^{3/2}\right]^{-1/3}. \tag{10}$$

The mode Grüneisen parameter $\gamma_j(\mathbf{q})$ describing the phonon frequency shift with respect to the volume can be expressed as

$$\gamma_j(\mathbf{q}) = -\frac{d[\ln \omega_j(\mathbf{q}, V)]}{d[\ln V]}. \tag{11}$$

The acoustic Grüneisen parameter $\gamma(T)$ is defined as the weighted average of the mode Grüneisen parameter for all acoustic phonon branches, which can be calculated by

$$\gamma(T) = \frac{\alpha_V(T)B(T)V_m(T)}{C_V(T)}, \tag{12}$$

where $\alpha_V(T)$ is the thermal expansion coefficient, $V_m(T)$ is the volume per mole, $B(T)$ is the bulk modulus, and $C_V(T)$ is the specific heat.

III. RESULTS

A. Structure and magnetic states

At room temperature and zero pressure conditions, CmO_2 crystallizes in a CaF_2-like ionic structure with space group $Fm\bar{3}m$ (No. 225) [28,59], which is shown in Fig. 1. Its cubic unit cell is composed of four CmO_2 formula units (f.u.) with the curium atoms and the oxygen atoms in $4a(0, 0, 0)$ and $8c(0.25, 0.25, 0.25)$ Wyckoff sites, respectively. In experiment [27], a phase transition to an orthorhombic structure at pressure range of 30–40 GPa has been reported. In the present work, we only study the ground-state fluorite phase. Since the magnetic structure of CmO_2 is still unclear in experiments [30] and most actinide dioxides are stable as a (100) AFM state [19,20,60–62], we should consider the NM, FM, and (100) AFM configurations in our following study. For simplicity, we label (100) AFM as AFM.

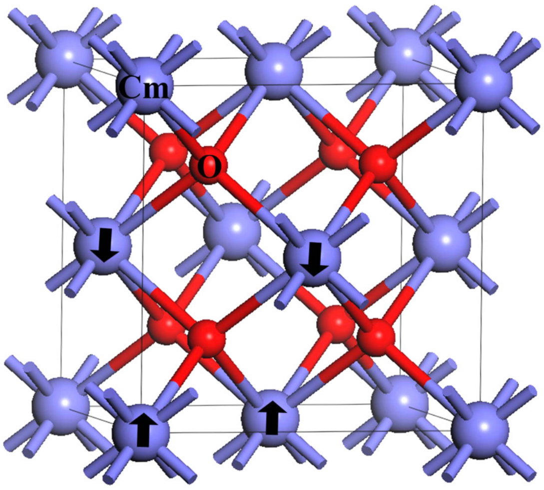

FIG. 1. Unit cell of fluorite CmO_2. Large violet atoms are Cm, while small red atoms are O. The black arrows illustrate the (100) AFM ordering.

As shown in Table I, the NM state of CmO_2 is not energetically favorable compared with the AFM and FM states. At the same time, the dependence of the total energy (per f.u. at respective optimum geometries) on U for both AFM and FM configurations is shown in Fig. 2. It is clear that the FM arrangement always has the lowest energy. Using a typical value of $U = 4$ eV, the total-energy differences ($\Delta E = E_{\mathrm{AFM}} - E_{\mathrm{FM}}$) are calculated to be 82, 25, 151, 68, 132, and 35 meV with GGA, LDA, GGA+U, LDA+U, GGA+U+SOC, and LDA+U+SOC, respectively. The strong Coulomb repulsion and/or the SOC have not turned over the stability of the magnetic states.

In Fig. 3, we compare our optimized a_0 and B with available experimental values [27,29]. While LDA underestimates the value of a_0, the GGA overestimates it. After including the strong Coulomb repulsion, with LDA+U, the a_0 is steadily increased to close to the experimental value with a typical value of $U = 3$ or 4 eV. Using $U = 4$ eV, the LDA+U gives $a_0 = 5.378$ (5.341) Å for the FM (AFM) state, which is close to the experimental value of 5.359 Å [29] as well as the SIC-LSD value of 5.37 Å [6].

We show in Fig. 4(a) the lattice constants of AFM AO_2 (A = U, Np, Pu, Am, and Cm) series. Results calculated with LDA+U [17,19,20] and LDA+U+SOC [20] are slightly smaller than the corresponding experimental values [29] but the trends agree, i.e., the lattice constants decrease almost linearly with increasing Z. This indicates that our results are believable. Through comparing, we note that the differences raised by including the SOC are very limited. On the whole, the LDA+U(+SOC) results are consistent with the HSE lattice constants [5,62], but smaller than the corresponding SIC-LSD lattice constants [6].

For bulk modulus B, as indicated in Fig. 3(b) and Table I, including the strong Coulomb repulsion Hubbard U parameter in our calculations will lead to a large offset with respect to

TABLE I. Equilibrium lattice constants (a_0), total energy (E), bulk modulus (B), pressure derivative of the bulk modulus (B'), and magnetic moments (μ_s and μ_l) for NM, FM, and AFM states of $\mathrm{CmO_2}$ calculated with GGA/LDA, GGA/LDA+U ($U = 4$ eV), and GGA/LDA+U+SOC ($U = 4$ eV) at 0 GPa. For comparison, experimental values and results from other calculations are also listed.

Mag.	Method	a_0 (Å)	E (eV)	B (GPa)	B'	$\mu_s(\mu_l)$ (μ_B)
NM	GGA	5.265	−32.582	198.6	4.4	
	GGA+U	5.381	−29.396	194.1	4.5	
	GGA+U+SOC	5.410	−37.538	193.3	4.4	
	LDA	5.149	−35.825	239.7	4.4	
	LDA+U	5.272	−32.304	230.3	4.4	
	LDA+U+SOC	5.303	−40.488	227.0	4.3	
FM	GGA	5.435	−36.217	162.5	4.9	6.13
	GGA+U	5.532	−35.093	129.5	4.5	6.60
	GGA+U+SOC	5.523	−39.390	129.6	4.7	6.41(−0.19)
	LDA	5.308	−38.526	207.1	4.8	5.91
	LDA+U	5.378	−37.168	167.9	4.8	6.37
	LDA+U+SOC	5.368	−41.600	170.2	4.8	5.94(−0.32)
AFM	GGA	5.419	−36.135	161.9	4.8	5.98
	GGA+U	5.503	−34.942	120.8	4.4	6.47
	GGA+U+SOC	5.490	−39.258	123.7	5.6	6.22(−0.33)
	LDA	5.287	−38.501	204.6	4.6	5.71
	LDA+U	5.341	−37.100	176.5	5.9	6.15
	LDA+U+SOC	5.332	−41.565	188.0	6.1	5.68(−0.52)
	Expt.	5.359[a]		218(5)[b]	7(1)[b]	
	FPLMTO[c]			218.0	3.1	
	SIC-LSD[d]	5.37		212		

[a] Reference [29].

[b] Reference [27].

[c] Reference [32].

[d] Reference [6].

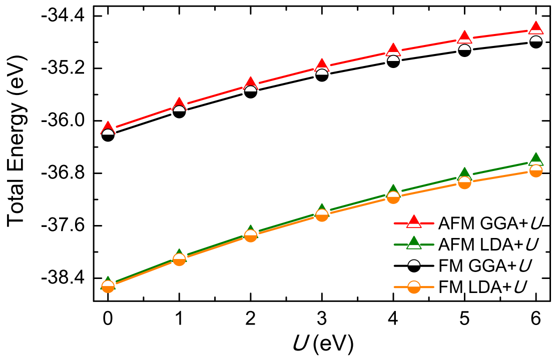

FIG. 2. Dependencies of the total energies (per f.u.) on U for FM and AFM states.

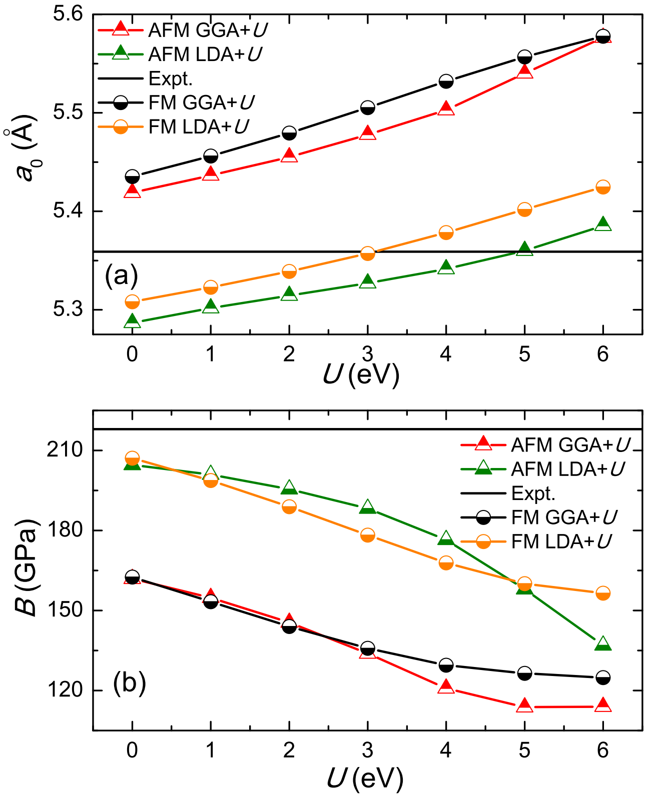

FIG. 3. Dependencies of the (a) lattice parameter and (b) bulk modulus on U for FM and AFM phases.

the experimental values [27] and theoretical values [6,32]. Here, one may doubt our results. However, concerning the old experimental values [27,63] of B for $A\mathrm{O_2}$, the results for $\mathrm{PuO_2}$ and $\mathrm{AmO_2}$ were found by a new experiment [64] to be largely overestimated. Besides, the high-pressure experiments [27] were performed at ambient temperature but our results are only valid at 0 K. A paramagnetic model [65] should be more reasonable to predict a smaller bulk modulus, however, this kind of calculation is outside of our present work. Anyway, our GGA+U calculations for NM, FM, and AFM states give $B = 194.1$, 129.5, 120.8 GPa, respectively, which are in good agreement with recent GGA+U calculations [37] ($B = 203.6$, 134.7, and 128.6 GPa, respectively). Thus further experimental and theoretical studies are needed before any general conclusions can be drawn about our calculated values of B. From Fig. 3(b), one can find that the LDA+U results (156 − 207 GPa)/(137 − 204 GPa) of FM/AFM state are always higher than the GGA results (125 − 162 GPa)/(114 − 162 GPa). This is understandable since the lattice constants are always overestimated using GGA. Using $U = 4$ eV, we obtain $B = 167.9/176.5$ GPa for the FM/AFM state with LDA+U. After including SOC, these values are increased to 170.2 and 188.0 GPa, respectively, which are closer to the experimental value of 218 GPa [27].

Assuming a $5f^6$ dominated configuration for Cm in a +4 valence state, a single-particle picture, according to the third Hund's rule, tells us the total momentum $\mathbf{J}$ would vanish. This picture is, of course, inappropriate due to various effects including crystal field splittings, covalency/hybridization effects, and the many-body nature of the local Cm moment. We can evaluate the spin and orbital contribution to the magnetic moment (μ_s and μ_l). In calculations, the direction of the magnetic moment is set along z axis. Results obtained with GGA/LDA, GGA/LDA+U, and GGA/LDA+U+SOC are tabulated in Table I. The values of μ_s with GGA/LDA+U are slightly larger than that with GGA/LDA and GGA/LDA+U+SOC. In particular, the

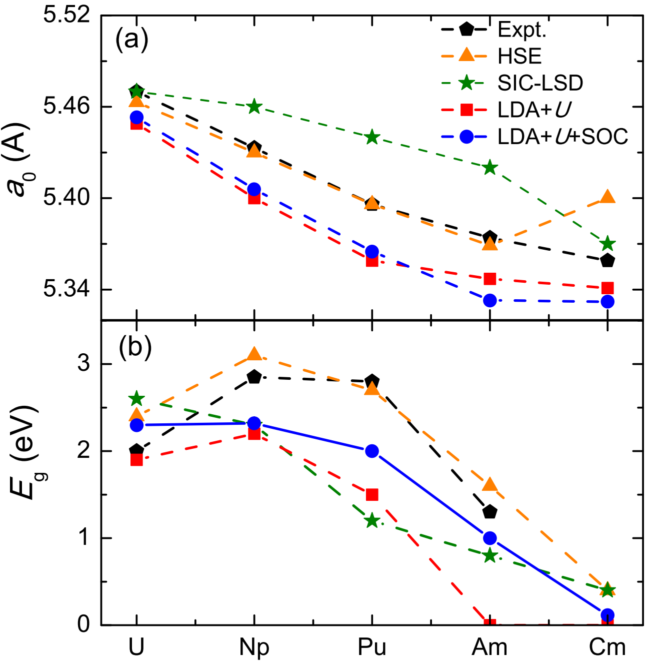

FIG. 4. (a) Lattice parameters and (b) band gaps of the actinide dioxides in the AFM state calculated with the LDA+U(+SOC) ($U = 4$ eV) methods. Some values are from our previous calculations [17,19,20]. Experimental values from Refs. [29,68–70], the SIC-LSD values from Ref. [6], and the HSE values from Refs. [5,62] are also shown for comparison.

LDA+U+SOC calculations give values of $\mu_s = 5.68\,\mu_B$ and $\mu_l = -0.52\,\mu_B$ for the AFM state, which result in a total magnetic moment $\mu_{\text{total}} = 5.16\,\mu_B$. These values are in good agreement with a previous DFT value of $\mu = 5.21\,\mu_B$ [6] with SIC-LSD, but larger than the experimental magnetic moment of $\mu_{\text{eff}} = 3.36 \pm 0.06\ \mu_B$ [30]. The difference between the calculations and the experiment need further clarification through neutron diffraction experiments, if a large enough sample can be obtained.

B. Electronic structure

For half-filled $5f$ electronic systems, the strong Coulomb repulsion effect as well as the relativistic effect of SOC are both critical in obtaining reasonable electronic structures. This fact has been well established in many actinide dioxides and hydrides [5,6,17,19,20,22,26,61,66,67]. For our present system CmO_2, although there are no experimental results to compare, the effects of strong Coulomb repulsion and SOC should be considered [5,6].

From our calculated electronic density of states (DOS), Figs. 5 and 6, one can find that including the strong Coulomb repulsion effect (using $U = 4$ eV) pushes the $5f$ electrons occupation from near the Fermi energy level (-2 to 0 eV) to a deeper energy level (-4 to -2 eV). The main occupation near the Fermi level is turned over from U $5f$ to O $2p$. The peak-type distribution of the $5f$ electrons is smoothed. This kind of electronic occupation is in good agreement with the result obtained with HSE [5]. For the FM state, we only obtain a half-metallic state even when we increase U to 6 eV. As for the AFM state, a metallic state is predicted with LDA+U while a charge-transfer semiconductor with an indirect band gap of 113 meV is obtained with LDA+U+SOC. This value of the band gap is smaller than previous calculated values of 0.4 eV with HSE [5] and SIC-LSD [6] as well as 0.57 eV with GGA+U+SOC ($U = 4$ eV) [37]. The origin of this discrepancy is unknown and needs further experiments to clarify. We also perform calculations for the NM state. Using GGA/LDA+U and GGA/LDA+U+SOC, we calculate the band gaps to be 1.90/1.80 and 1.94/2.02 eV, respectively, which are close to previous calculated values of ~2 eV with LDA+U [35].

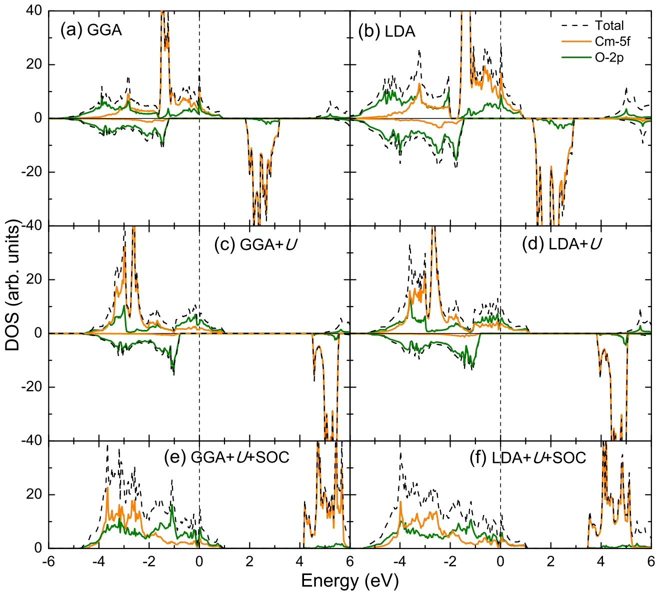

FIG. 5. The total and the orbital-resolved local DOSs for the FM state calculated with GGA/LDA, GGA/LDA+U, GGA/LDA+U+SOC using $U = 4$ eV. The Fermi energy level is set at zero.

For band gaps of the AFM state in the $A\text{O}_2$ series, compared with LDA+U [17,19,20], using LDA+U+SOC [20] could result in better consistency with the experiments [68–70] [see

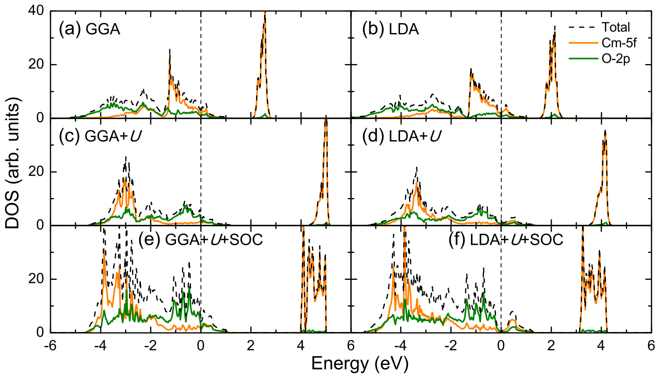

FIG. 6. The total and the orbital-resolved local DOSs for the AFM state calculated with GGA/LDA, GGA/LDA+U, GGA/LDA+U+SOC using $U = 4$ eV. The Fermi energy level is set at zero.

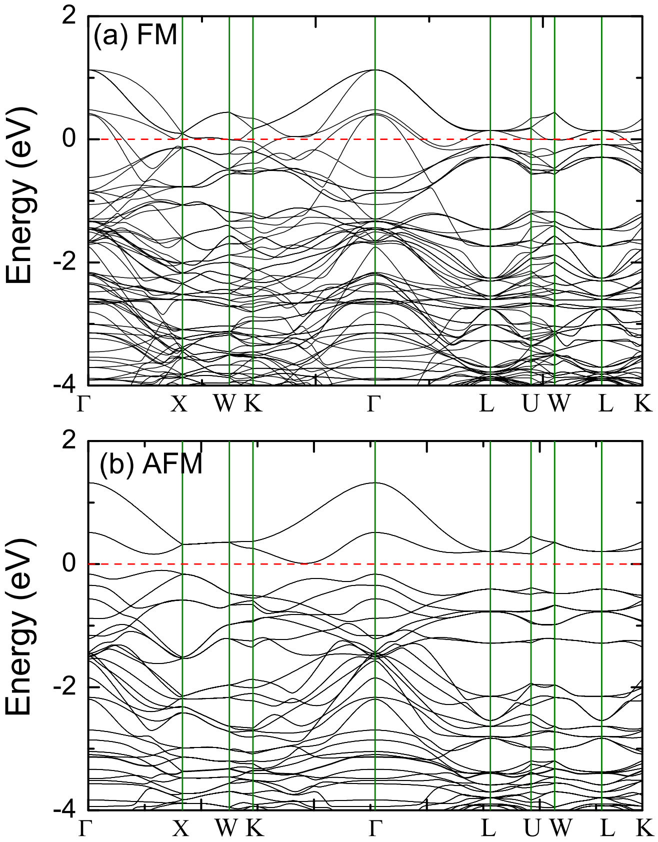

FIG. 7. The band structures for FM and AFM states calculated with LDA+U+SOC using $U = 4$ eV. The Fermi energy level is set at zero.

Fig. 4(b)]. The trends, first increase from UO_2 to NpO_2 and then decrease from PuO_2 to CmO_2, agree fairly well with experiments. This indicates that our results are believable. The largest discrepancy between the LDA+U calculations and experiments occurs for PuO_2 and AmO_2, where the gaps differ by some 1.3 eV. A zero band gap is predicted with LDA+U for AmO_2 and CmO_2. On the whole, the LDA+U+SOC results are consistent with the SIC-LSD band gaps [6], but smaller than the corresponding HSE gaps [5,62]. Therefore the effects of the SOC on the electronic structures as well as the global minimum are crucial for AO_2 [20,62,71].

To clearly view the electronic structure, we plot in Fig. 7 the band structure of the FM and AFM states calculated with LDA+U+SOC. For the metallic FM state, there are at least three bands that cross the Fermi level along the Γ-X, Γ-K, Γ-L, L-K, and W-K high-symmetry directions, which results in a three-dimensional conductivity. For the semiconducting AFM state, the conduction-band minimum is located along the Γ-K line and the valence-band maximum along the Γ-X line.

C. Elasticity and chemical bonding

As indicated in Refs. [20,71] for typical actinide dioxides, the effects of the SOC on the elastic properties, phonon spectrum, and thermodynamic properties can be neglected. Thus, in the following, we will present results obtained without SOC.

The elastic constant, various moduli, Poisson's ratio, density, elastic wave velocities, and Debye temperatures for FM and AFM states are presented in Table II. Obviously, both AFM and FM states of CmO_2 are mechanically stable because their elastic constants satisfy the mechanical stability criteria [72] of the cubic structure: $C_{11} > 0$, $C_{44} > 0$, $C_{11} > |C_{12}|$, $(C_{11} + 2C_{12}) > 0$. The derived bulk moduli for FM/AFM calculated with GGA/LDA(+U) are close to that obtained by the EOS fitting. The discrepancies between these two methods are within 4 GPa. This means that our calculations are consistent and reliable. We note that our calculated C_{11}, C_{12}, C_{44} are smaller by 81.8, 15.9, and 12.8 GPa compared to a recent GGA+U study [37]. Their derived bulk modulus ($B = 160.730$ GPa) from elastic constants is inconsistent with their EOS fitting result ($B = 128.62$ GPa). So, our results are more reliable.

To understand the elastic properties of CmO_2 in AO_2 series, we compare in Table III the elastic constants, elastic moduli, elastic wave velocities, and Debye temperature of CmO_2 with corresponding results of other actinide dioxides [17,19,20,25]. The results of the NM ThO_2 [25] were calculated with GGA while the results of UO_2 to CmO_2 in the AFM state were/are obtained with LDA+U ($U = 4$ eV) [17,19,20]. We only compare the results for the AFM state (UO_2 to CmO_2) which is the most stable magnetic configuration for most AO_2. Among these AO_2 series, the values of the elastic constants and the elastic moduli for CmO_2 are the smallest. This is partially due to the fact that the number of $5f$ electrons is increased from U to Cm. Another reason may find its answer from analyzing their electronic DOS. For middle AO_2, PuO_2 [19], and AmO_2 [26], the degeneracy of the $5f$-$2p$ orbitals in the energy below the Fermi level is dominant. However, this kind of degeneracy is very weak for UO_2 [20], NpO_2 [17], and CmO_2. This kind of orbital mixing and covalency has also been noticed in a previous HSE study [5].

The elastic properties of materials is tightly related to their chemical bonding. To study the chemical bonding for CmO_2, we plot the isosurfaces of the charge density and difference charge density in Fig. 8. While the two-dimensional isofurfaces are plotted in the $(1\bar{1}0)$ plane, the three-dimensional one is viewed along the [001] direction. The difference charge density is obtained by subtracting the densities of noninteracting component systems, $\rho(\mathrm{Cm})+\rho(\mathrm{O})$, from the density of the CmO_2, while maintaining the positions of the component systems at the same location as in CmO_2. These pictures are obtained for the FM state with LDA+U ($U = 4$ eV). As indicated in Fig. 8(a), the charge densities around the Cm and O ions have almost a spherical distribution with a slightly deformed distribution towards their nearest neighboring atoms to form the Cm-O bonding. It is the network of these Cm-O bonds that is responsible for the stability. We will carefully investigate the ionic/covalent natures of the Cm-O bonds in the following. The charge density around Cm and O ions is high while there are almost no remaining charges in the large octahedral-hole interstitial region. From the two-dimensional and three-dimensional isosurfaces of the difference charge density, presented in Figs. 8(b) and 8(c), respectively, we find that the main contribution to the charge accumulation is from O atoms, not Cm.

TABLE II. Elastic constants (C_{11}, C_{12}, C_{44}), bulk modulus (B), shear modulus (G), Young's modulus (E), Poisson's ratio (ν), density (ρ), transverse (υ_t), longitudinal (υ_l), average (υ_m) sound velocity, and Debye temperature (θ_D) for FM and AFM states with GGA/LDA and GGA/LDA+U ($U = 4$ eV).

Magnetism	Method	C_{11} (GPa)	C_{12} (GPa)	C_{44} (GPa)	B (GPa)	G (GPa)	E (GPa)	ν	ρ (g/cm^3)	υ_t (m/s)	υ_l (m/s)	υ_m (m/s)	θ_D (K)
FM	GGA	289.4	102.8	35.1	165.0	52.6	142.6	0.356	11.546	2134.4	4513.0	2401.6	301.4
	GGA+U	207.8	92.4	38.7	130.8	45.4	122.2	0.344	10.951	2037.4	4181.2	2289.0	282.2
	LDA	355.6	137.1	54.6	209.9	72.4	194.7	0.345	12.395	2416.2	4972.0	2715.0	348.8
	LDA+U	279.9	114.9	47.2	169.9	59.2	159.0	0.344	11.914	2228.2	4569.5	2503.2	317.4
AFM	GGA	298.0	97.8	19.1	164.5	39.9	110.7	0.388	11.650	2841.6	4323.0	3112.0	391.0
	GGA+U	199.6	84.5	14.0	122.9	25.8	72.2	0.402	11.125	1521.8	3759.3	1723.2	213.6
	LDA	367.2	127.4	43.7	207.3	66.4	180.0	0.355	12.545	2300.6	4856.0	2588.5	333.9
	LDA+U	312.8	113.4	36.0	179.9	54.9	149.4	0.362	12.165	2124.0	4561.0	2391.8	305.4

To study the covalent and ionic characters quantitatively, we calculate the line charge density along the Cm-Cm, Cm-O, and O-O bonds and also perform the Bader analysis. The Bader charges, Bader volumes, bond lengths, and line charge density at the corresponding bond points (CD$_b$) are listed in Table IV. From these results, we can deduce some points for CmO$_2$: i> The CmO$_2$ is bonded by Cm-O mixed covalent and ionic bonds. The CD$_b$ value for Cm-O of 0.064–0.081 e/au^3 for the FM state and 0.066–0.083 e/au^3 for the AFM state are lower than 0.104 e/au^3 found for the Si covalent bond [73], but prominently higher than 0.007 e/au^3 found for the Na-Cl bond in the typical ionic crystal NaCl [73]. Besides, from our calculated Bader charges, we find that each Cm atom loses 2.20–2.26 (2.20–2.26) electrons to O atoms for the FM (AFM) state. The ionic charge for FM and AFM states of CmO$_2$ can be represented as $\text{Cm}^{2.20+}\text{O}^{1.10-}$ and $\text{Cm}^{2.26+}\text{O}^{1.13-}$, respectively; ii> the differences between AFM and FM are very small; iii> the effects brought by the strong Coulomb repulsion are also limited. After including Hubbard U, the bond lengths are increased and the CD$_b$ are decreased. In addition, the covalent property as presented by the value of the CD$_b$ (around 0.53 $e/\text{Å}^3$ for AFM state with LDA+U) for CmO$_2$ is comparable to that for UO$_2$, NpO$_2$, and PuO$_2$ [19]. The ionicity of AO$_2$ is again found to show a decreasing trend with increasing Z [19].

D. Phonon dispersion

Employing the Hellmann-Feynman theorem and the direct method, we have calculated the phonon curves along Γ-X-W-K-Γ- L-U-W-L directions in the BZ as well as the PhDOS, which are displayed in Fig. 9 for FM and AFM states with LDA+U ($U = 4$ eV). To our knowledge, there are no experimental and theoretical phonon results available in literature for CmO$_2$. Our previously reported phonon curves and/or PhDOS for PuO$_2$ [19] and UO$_2$ [20] have been examined recently by experiments [9,12,21] showing good agreements. So, our present phonon results for CmO$_2$ may find their instructive significance for experiments and theoretical calculations in the future. Besides, the Born effective charges, responsible for the longitudinal optical (LO)-transverse optical (TO) splitting near the Γ point in BZ, of Cm and O ions for FM (AFM) state are calculated to be $Z^*_{\text{Cm}} = 1.07$ (4.41) and $Z^*_{\text{O}} = -0.46$ (-2.19), respectively. The values for the AFM state are comparable with NpO$_2$, PuO$_2$, UO$_2$, and AmO$_2$ [17,19,20,26].

In the primitive cell of the fluorite CmO$_2$, there are only three atoms (one Cm and two O atoms). So, there are nine phonon modes in the phonon dispersion. We can see that there appears a phonon gap between the optic modes and the acoustic branches of about 2.1 (2.0) THz for the FM (AFM) state. This kind of phonon gap has never been found in other AO$_2$ for A = Th to Am [17,19,20,25,26]. Because curium atoms are

TABLE III. Elastic constants (C_{11}, C_{12}, C_{44}), bulk modulus (B), shear modulus (G), Young's modulus (E), Poisson's ratio (ν), density (ρ), transverse (υ_t), longitudinal (υ_l), average (υ_m) sound velocity, and Debye temperature (θ_D) for AFM state. For comparison, the theoretical results of other actinide dioxides (AmO$_2$, PuO$_2$, NpO$_2$, UO$_2$, ThO$_2$) with LDA+U ($U = 4$ eV) are also listed.

	C_{11} (GPa)	C_{12} (GPa)	C_{44} (GPa)	B (GPa)	G (GPa)	E (GPa)	ν	ρ (g/cm^3)	υ_t (m/s)	υ_l (m/s)	υ_m (m/s)	θ_D (K)
ThO$_2$[a]	349.5	111.4	70.6	191	87.1	226.8	0.302	9.880	2969.1	5575.5	3317.3	402.6
UO$_2$[b]	389.3	138.9	71.3	222.4	89.5	236.7	0.323	11.084	2841.8	5552.7	3183.4	398.1
NpO$_2$[c]	399.5	145.5	72.9	230	91.2	241.7	0.325	11.351	2834.6	5565.6	3176.4	401.2
PuO$_2$[d]	319.6	177.8	74.5	225	73.0	197.7	0.354	11.896	2477.9	5205.8	2787.2	354.5
AmO$_2$	352.9	109.9	80.0	190.9	94.6	243.6	0.287	11.953	2813.7	5150.5	3137.8	400.2
CmO$_2$	312.8	113.4	36.0	179.9	54.9	149.4	0.362	12.165	2124.0	4561.0	2391.8	305.4

[a] Results of NM state with GGA method from Ref. [25].

[b] Reference [20].

[c] Reference [17].

[d] Reference [19].

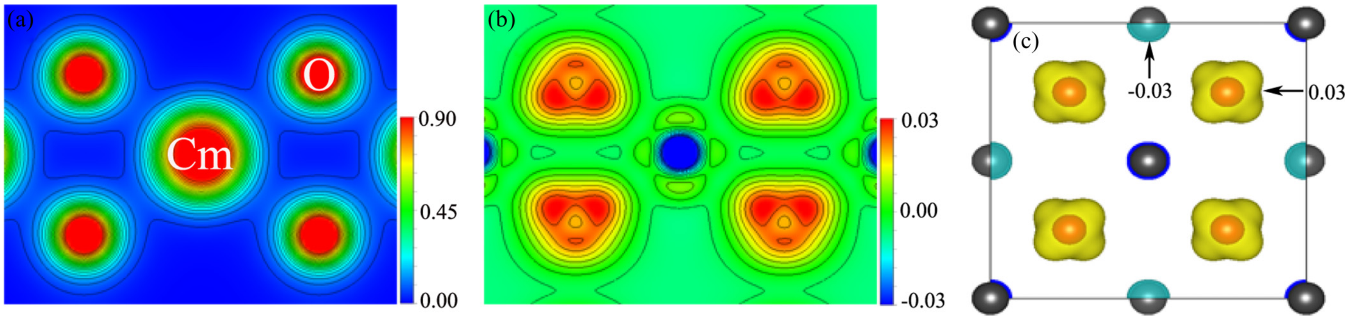

FIG. 8. (a) Valence charge density and (b) difference charge density of FM state in the $(1\bar{1}0)$ plane calculated with LDA+U using $U = 4$ eV. The contour lines for the valence charge density are drawn from 0.0 to 0.8 at 0.05 e/au^3 intervals while for the difference charge density are drawn from −0.03 to 0.03 at 0.005 e/au^3 intervals. In (c), we show a three-dimensional isosurface for the difference charge density.

heavier than these actinides, the appearance of the phonon gap is understandable. The phonon frequencies of AFM state are larger than that of FM state, especially for the two LO modes. This is due to the fact that the lattice constants of the AFM state are smaller than that of FM state. Since the amplitudes of the Born effective charges of the AFM state are dramatically larger than that of the FM state, the LO-TO splitting in the AFM state is evident while in the FM state is almost invisible. Besides, the PhDOS of the FM (AFM) can be viewed as two parts. One part is lower than 4.8 (5.3) THz with the main contribution coming from the curium sublattice while the other part is higher than 6.9 (7.3) THz with the main contribution from the oxygen sublattice.

E. Thermodynamic properties

Using $U = 4$ eV within LDA+U, the free energy curves $F(T,V)$ for temperatures ranging from 0 up to 2000 K for FM and AFM states are calculated (see Fig. 10). Within QHA [51], the ground-state total energy $E(V)$ and the phonon free energy $F_{\text{ph}}(T,V)$ are calculated by constructing several $2 \times 2 \times 2$ supercells. From our calculated $F(T,V)$ at several constant temperatures, without or with considering the thermal electronic contribution $F_{\text{el}}(T,V)$, the equilibrium lattice parameter $a(T)$ and bulk modulus $B(T)$ are obtained by EOS fitting and are presented in Fig. 11. The thermal-expansion coefficients $\alpha_V(T)$ are presented in Fig. 12 together with the experimental results [74,75] and other theoretical results [31]. The $a(T)$ with the contribution of the F_{el} are also shown in Fig. 10.

As shown in Fig. 11(a), the lattice parameters $a(T)$ for both magnetic states increase steadily upon increasing temperature. This kind of expansion has also been observed in our previous study of PuO_2 [19] and UO_2 [20]. The effect of the thermal electronic contribution for the AFM state is very strong while that for the FM state is weak. This is because the values of $D(\epsilon_F)$ for the FM state are almost constant upon changing volumes while that for the AFM state increase dramatically with increasing volumes. Increasing the temperature over about 1500 K, the $a(T)$ values for the AFM state are turned to larger than those for the FM state. Our calculated values of $\alpha_V(T)$ are larger than the experimental results [74,75] but the trends agree.

For bulk modulus $B(T)$, evident decreasing behaviors are found with increasing temperature for both FM and AFM states. The effect of the thermal electronic contribution here is very weak. Specifically, the amplitude of such a change between 0 and 1500 K for the AFM state of CmO_2 is ∼70.3 GPa, which is larger than that of UO_2 [20] and PuO_2 [19] by about 43.5 and 49.7 GPa, respectively. This fact indicates that CmO_2 will be softened quicker upon increasing temperature in comparison with UO_2 and PuO_2.

The calculated specific heat at constant volume C_V, specific heat at constant pressure C_P, and entropy S are shown in Fig. 13. In calculating the C_P, the thermal electronic contribution has been included. It can be seen that the C_V increases quickly up to room temperature and becomes close to a constant in the Dulong-Petit limit [76]. Over the Debye temperature, the C_P increases continuously. In the temperature

TABLE IV. Calculated charge (Q_B) and volumes (V_B) according to Bader partitioning as well as the bond lengths and charge density values at bond points (CD_b) for FM and AFM states with GGA/LDA and GGA/LDA+U ($U = 4$ eV) approaches.

Magnetism	Methods	Q_B(Cm) (e)	Q_B(O) (e)	V_B(Cm) (Å^3)	V_B(O) (Å^3)	Cm-Cm (Å)	Cm-O (Å)	O-O (Å)	CD_b(Cm-Cm) (e/au^3)	CD_b(Cm-O) (e/au^3)	CD_b(O-O) (e/au^3)
FM	GGA	15.74	7.13	15.40	12.37	3.843	2.354	2.718	0.022	0.072	0.0022
	GGA+U	15.79	7.10	16.10	13.11	3.912	2.395	2.766	0.020	0.064	0.0019
	LDA	15.78	7.11	14.72	11.33	3.753	2.298	2.654	0.026	0.081	0.0028
	LDA+U	15.80	7.10	15.16	11.87	3.803	2.329	2.689	0.024	0.075	0.0025
AFM	GGA	15.74	7.13	15.41	12.18	3.832	2.346	2.709	0.022	0.073	0.0023
	GGA+U	15.75	7.13	15.92	12.87	3.891	2.383	2.751	0.021	0.066	0.0020
	LDA	15.80	7.10	14.70	11.12	3.738	2.289	2.643	0.026	0.083	0.0029
	LDA+U	15.74	7.13	14.92	11.59	3.777	2.313	2.671	0.025	0.078	0.0026

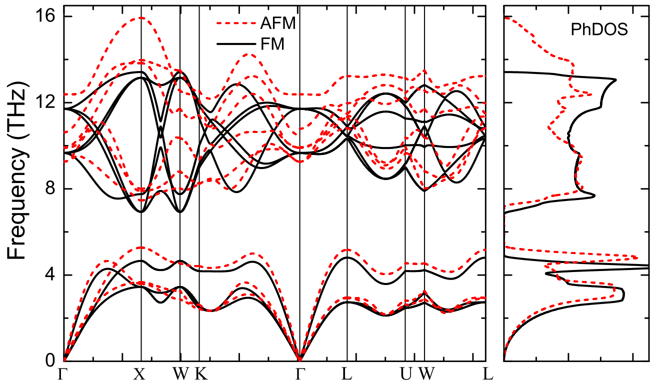

FIG. 9. Phonon dispersion curves (left) and corresponding PhDOS (right) for the AFM and FM states calculated with LDA+U using $U = 4$ eV.

range of 300–650 K, our calculated values of C_P agree well with experiment [28] and other theoretical results [31,77]. We never find evident differences between the FM and AFM states for $T < 900$ K, over which the differences become larger and lager with increasing temperature. This kind of temperature effect originates from the aforementioned difference of the thermal electronic contributions between these two magnetic states. The temperature-dependent behaviors of the S are similar with that of other $A\mathrm{O}_2$, such as UO_2 [20]. Over 50 K, the S of CmO_2 becomes slightly larger than that of UO_2. The electronic contribution to the S is very small, only about 1% of the lattice contribution. The differences between the FM and AFM states are limited.

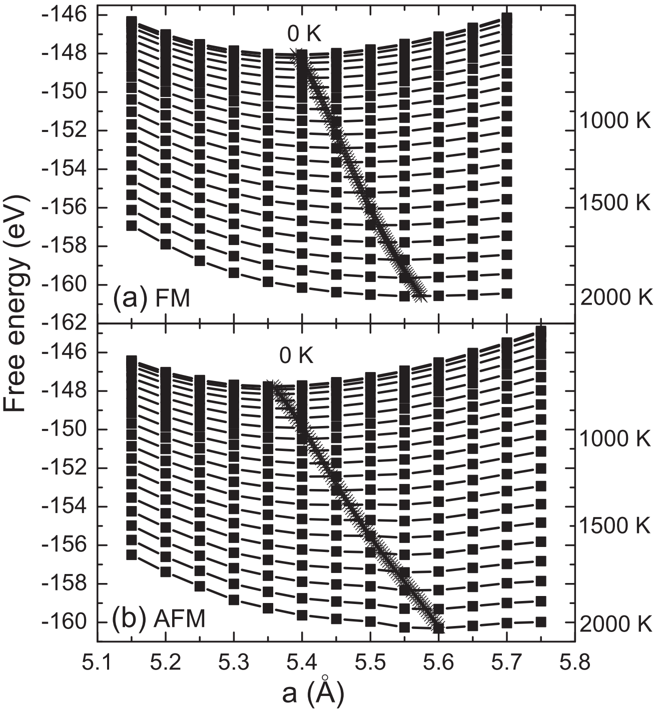

FIG. 10. Dependencies of the free energy $F(T,V)$ on the lattice parameter a at various temperatures for (a) FM and (b) AFM states calculated with LDA+U using $U = 4$ eV.

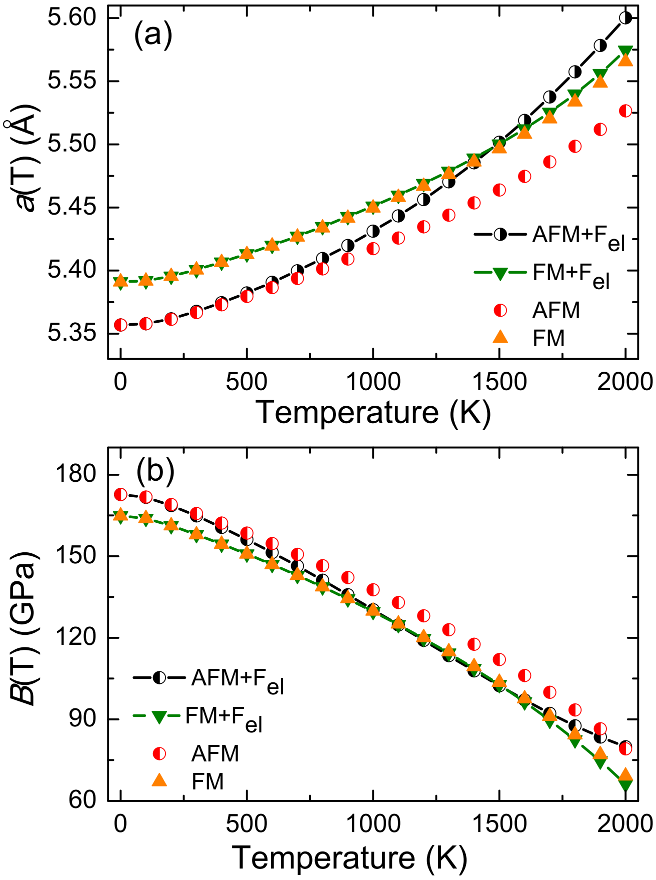

FIG. 11. Temperature dependencies of (a) lattice parameter $a(T)$ and (b) bulk modulus $B(T)$ for FM and AFM states with and without the electronic contribution.

In order to discuss the anharmonic effects in CmO_2, we calculate the Grüneisen parameters for each vibration mode $\gamma_j(\mathbf{q})$ according to Eq. (11) by expanding and compressing the equilibrium volume ∼1%. Based upon our calculated

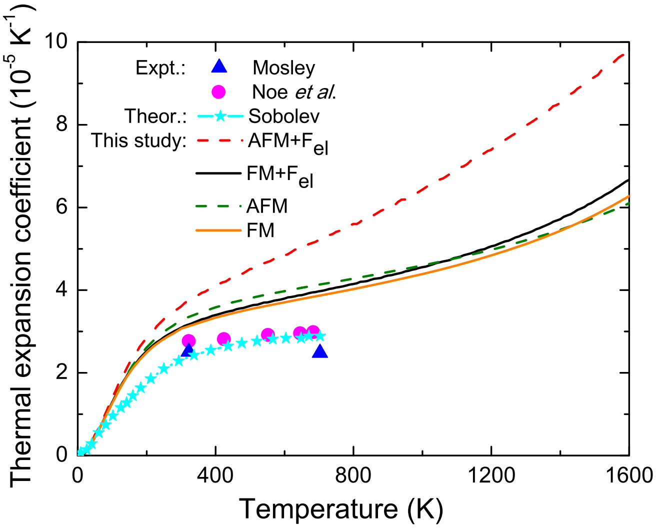

FIG. 12. Temperature dependencies of thermal expansion coefficients for FM and AFM states with and without the electronic contribution. Experimental results from Refs. [74,75] and other theoretical results from Ref. [31] are also shown for comparison.

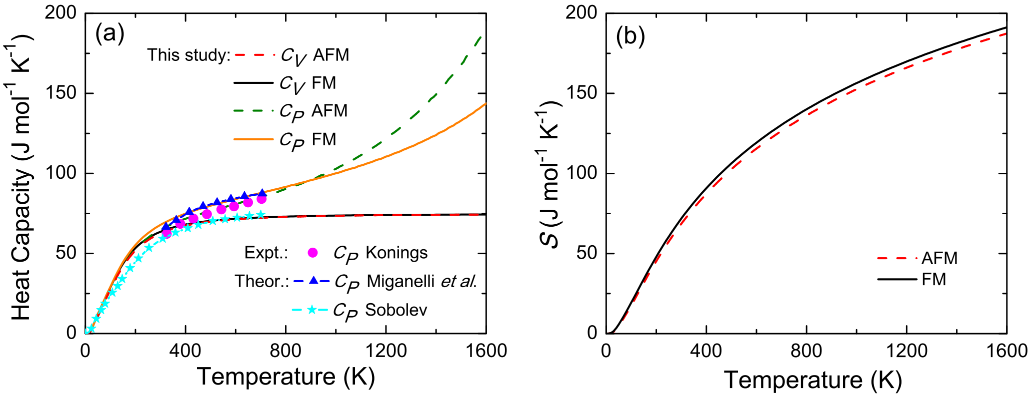

FIG. 13. Temperature dependencies of (a) specific heat at constant volume (C_V) and constant pressure (C_P) as well as (b) entropy for FM and AFM states. Experimental [28] and other theoretical [31,77] results of C_P are presented.

phonon spectra, we plot the mode Grüneisen parameters along Γ-X-W-K-Γ-L-U-W-L directions in Figs. 14(a) and 14(b) for the FM and AFM states, respectively.

For the FM state, we find that the second optical branches (TO1′, TO2′ and LO′) of the Grüneisen parameters have some negative values near the Γ point. All other branches are positive in the whole BZ. At U point, the largest value of the mode Grüneisen parameter appears on the first transverse optical branches (TO1), close to 2.4. All the branches distribute mainly in range from 0.5 to about 2.4. As for the AFM state, the first optical branches (TO1, TO2, and LO) have some negative values near the Γ point. The largest value of about 3.8 appears at L point for the LO′ mode. The main distribution of $\gamma_j(\mathbf{q})$ is in range from 1.2 to 3.3. This fact indicates that the anharmonic effect in the AFM state is stronger than that in the FM state.

To quantitatively analyze the anharmonic effects along typical crystalline directions, we calculate the average mode Grüneisen parameters $\bar{\gamma}_j$ along the Γ-X, Γ-K, and Γ-L directions through $\bar{\gamma}_j = \sum \gamma_j(\mathbf{q}) / \sum(\mathbf{q})$ and present them in Table V. The Γ-X, Γ-K, and Γ-L in BZ stand for the [001], [110], and [111] orientations of the CmO_2 unit cell, respectively. As indicated in Table V, the largest average value for the FM state appears on the TO1 branch along the [011] direction, while for the AFM state is on the LO′ branch along the [111] direction. These results illustrate large anharmonicity

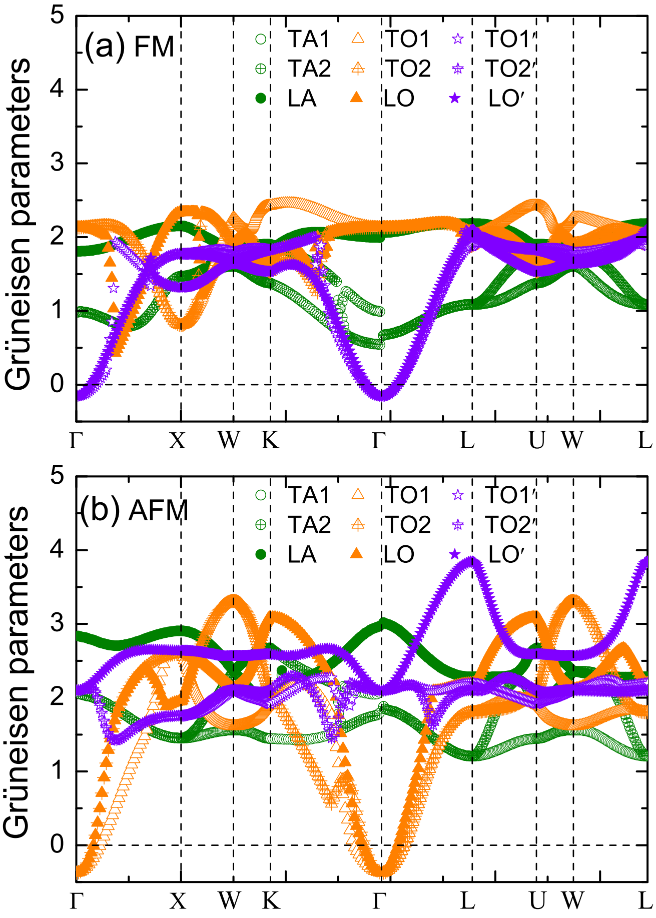

FIG. 14. Theoretically calculated Grüneisen dispersions along high-symmetry directions in the reciprocal lattice space for (a) FM and (b) AFM states. The acoustic branches, circles; the first optical branches, triangles; the second optical branches, pentagrams.

TABLE V. The average mode Grüneisen parameters $\bar{\gamma}_j$ and group velocities $\upsilon_j(\times\ 10^2\ \mathrm{m/s})$ of FM and AFM states along the [001], [011], and [111] crystal directions. Since the symmetry along the [001] and [111] directions is high, the two transverse vibration branches are degenerated, thus, they are presented as one value.

Branch	FM					
	$\bar{\gamma}_j$			υ_j		
	[001]	[011]	[111]	[001]	[011]	[111]
TA	0.99	1.10/1.30	0.88	5.13	3.40/4.11	3.16
LA	1.92	2.01	2.10	6.97	4.46	5.53
TO	1.74	2.31/1.84	2.15	−3.89	−2.05/−1.57	0.92
LO	1.70	1.93	2.12	−2.68	−1.29	1.09
TO′	1.08	1.13/1.14	0.86	2.34	0.90/0.98	−1.24
LO′	0.90	1.00	0.94	2.79	1.81	−0.75
	AFM					
TA	1.70	1.69/2.06	1.49	5.34	3.56/4.38	3.32
LA	2.74	2.53	2.54	7.79	4.97	5.90
TO	1.46	1.35/0.98	0.94	−1.79	−1.17/−0.58	1.09
LO	1.55	1.87	1.33	−2.10	0.63	2.76
TO′	1.74	2.11/2.06	2.08	5.87	3.43/3.94	1.59
LO′	2.49	2.50	3.01	8.96	5.70	3.84

of the TO1 mode for the FM state and the LO′ mode for the AFM state. From Table V, we can summarize the Grüneisen parameter values on nine branches and along the three typical crystalline directions. We obtain $\bar{\gamma}(\mathrm{CmO_2}) = 38.84/49.63$ for the FM/AFM state. The result of AFM CmO_2 is slightly larger than that of AFM UO_2 [$\bar{\gamma}(\mathrm{UO_2}) = 46.06$] but smaller than that of AFM PuO_2 [$\bar{\gamma}(\mathrm{PuO_2}) = 61.86$] [78]. Thus we can say that the anharmonic effect of CmO_2 is comparable with UO_2 but is weaker than that of PuO_2. Understanding of the anharmonic effect is critical for our following study of the thermal conductivity.

The thermal conductivity of actinides plays important role in nuclear industries. To study the lattice thermal conductivity, we firstly analyze the phonon group velocities υ_j, $\upsilon_j = \frac{d\omega_j(\mathbf{q})}{d\mathbf{q}}$, since their tight relationship of $\kappa_L \propto \upsilon_j$. We deduce the phonon group velocities υ_j of FM and AFM states along the [001], [011], and [111] crystalline directions by utilizing the phonon spectra data $\omega_j(\mathbf{q})$ in Fig. 9 and present them in Table V. As seen in Table V, only the TA and LA branches of the FM state exhibit larger phonon group velocities than other branches while for the AFM state the TA, LA, TO′, and LO′ branches show relatively large phonon group velocities, especially along the [001] direction. These phonon modes should be regarded as good heat carriers. However, the large anharmonic effect may constrain the heat-transfer ability at high temperature, such as the LO′ mode for the AFM state.

After summarizing, we obtain the total phonon group velocities of FM (AFM) CmO_2 along the [001], [011], and [111] directions to be $35.16(44.85) \times 10^2$, $20.57(28.36) \times 10^2$, and $18.01(24.50) \times 10^2$ m/s, respectively. These data clearly indicate that the AFM CmO_2 shows larger phonon group velocities than FM CmO_2. The result of AFM CmO_2 is slightly larger than that of AFM UO_2 (39.42×10^2, 26.60×10^2, and 20.90×10^2 m/s, respectively) but smaller than that of AFM PuO_2 (62.87×10^2, 39.6×10^2, and 25.73×10^2 m/s, respectively) [78].

After the aforementioned analysis, one can believe that the acoustic branches of the two magnetic states play critical role in heat transfer no matter at low or high temperatures. However, the optical modes may only contribute mainly to the heat transfer at low temperatures. Their contribution at high temperatures is limited by the anharmonic-induced shorter mean free path. After ignoring the contribution from optical branches, we calculate the thermal conductivity for the FM and AFM states in the temperature range of 300–1600 K by the Slack relation and plot them in Fig. 15.

At 300 K, our calculated k_L for the AFM (FM) state is 8.6 (14.2) $\mathrm{W\,m^{-1}\,K^{-1}}$. The value of the AFM CmO_2 is in good agreement with the experimental value of 7–10 $\mathrm{W\,m^{-1}\,K^{-1}}$ at 298.15 K [28]. The value of the FM state is very large. This is because our calculated values of the Grüneisen parameters for the FM state are smaller than those for the AFM state. At room temperature, the actual experimental sample of CmO_2 may be the paramagnetic state. Thus the AFM model is more suitable than the FM model. With increasing temperature to 650 K, the experimental value of 3.8–4.6 $\mathrm{W\,m^{-1}\,K^{-1}}$ [28] is well in between our calculated k_L for the AFM (2.8 $\mathrm{W\,m^{-1}\,K^{-1}}$) and the FM (5.5 $\mathrm{W\,m^{-1}\,K^{-1}}$) states. From 300 to 650 K, most values of the theoretical results [31] are also in between our results for the AFM and FM states. Comparing with other AO_2 [78,79], the thermal conductivity of AFM CmO_2 in the temperature range of 300–650 K decreases more rapidly than that of ThO_2 and PuO_2, comparable to UO_2. Above 650 K, same with other AO_2, the decreasing behavior of k_L is more slow.

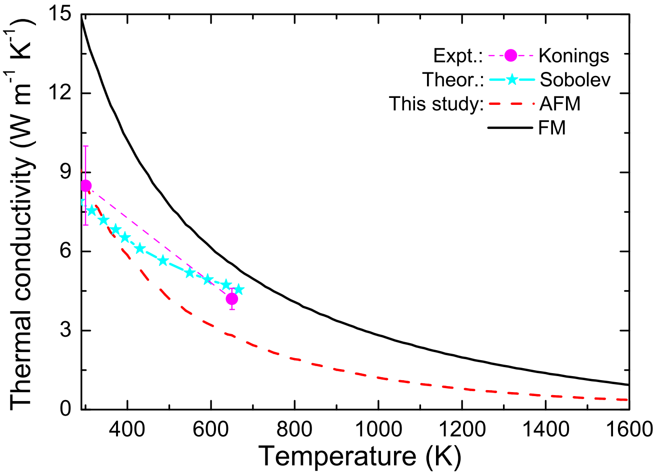

FIG. 15. Theoretically calculated lattice thermal conductivity for the FM and AFM states, together with available experimental [28] and other theoretical [31] results.

IV. DISCUSSION

CmO_2 is a member of actinides and has rich physics to explore. However, there are very limited reports on the investigation of this important $5f$ strong correlated system. Our first-principles simulations here give a detail analysis on the strong Coulomb repulsion and the SOC effects for CmO_2. Without including the Coulomb repulsion, using pure LDA or GGA, a localized distribution of the $5f$ orbitals above the O-$2p$ orbitals is observed and a metallic state is predicted for all considered magnetic states. After including the Coulomb repulsion, both LDA+U and GGA+U still result in a metallic state but with localized $5f$ orbitals below the O-$2p$ orbitals. Only by using LDA+U+SOC can one obtain the charge-transfer semiconductor state for the AFM configuration, consistent with previous HSE [5,62] and SIC-LSD [6] results. Through careful comparison, the FM state with half-metallic character is predicted to be energetically stable. This fact is different with many other AO_2, of which the AFM state is predicted to be more stable. For both AFM and FM states, our calculated elastic constants and phonon spectra indicate that they are mechanically and dynamically stable. Compared with experiments [27,29,30], our LDA+U(+SOC) calculations can predict reasonable results of lattice parameters and magnetic moments. In comparing with other AO_2, we present reasonable results of the lattice parameters, magnetic states, electronic density of states, band gaps, and elastic constants. We find that including both Coulomb repulsion and SOC is necessary in the study of global minimum magnetic states and reasonable electronic structures for many AO_2. In the study of macroscopic properties like elasticity and thermodynamics, the SOC can be neglected [20,71].

Using LDA+U, we present phonon spectra and various thermodynamic data for CmO_2, as it is a member of nuclear materials. Most of these data are firstly reported, such as the phonon spectra, Gibbs free energy, Grüneisen parameters, and phonon group velocities. Our results indicate that the DFT at the level of LDA+U approach works well to simulate these thermodynamic properties and can be easily extended to other systems, like U_3O_8 and U_2O_5.

V. CONCLUSION

In summary, the ground-state properties of CmO_2 are explored with first-principles LDA/GGA+U approaches. We calculate the equilibrium lattice parameters, bulk modulus, and one-electron behaviors of $5f$ states with different values of the Coulomb repulsion parameter U. By choosing the Hubbard U parameter around 4 eV within the LDA+U approach, the calculated lattice parameters for the FM and AFM states are in good agreement with experiments. For the energetically stable FM state, we only predict a metallic state no matter if we increase U to 6 eV or include SOC in our calculations. The main electronic occupation near the Fermi level is turned over by the strong Coulomb repulsion from U $5f$ to O $2p$. Same with our previous reports of other AO_2 [17,19,20,25,26], the Cm-O bonds in CmO_2 also can be interpreted as displaying a mixed ionic/covalent character. The stability of the two magnetic phases is predicted through calculation of elastic constants and phonon dispersion. Among AO_2, a phonon gap of ∼2 THz is firstly reported for CmO_2 and needs further experiments to verify. Based on our calculated E-V data, phonon spectra, and electronic density of states at the Fermi level, we obtain the Gibbs free energy, thermal expansion coefficient, specific heat, entropy, Grüneisen parameters, phonon group velocities, and lattice thermal conductivity. The effect of the thermal electronic contribution on some of these properties for the AFM state is very strong while that for the FM state is weak. In the temperature range of 300–650 K, our calculated values of C_P agree well with experiment [28]. The anharmonic effect of AFM CmO_2 is comparable with UO_2 but is weaker than that of PuO_2 [78]. Our calculated k_L at 300 K for the AFM state is in good agreement with experiment [28].

ACKNOWLEDGMENTS

B.T.W. thanks Weiwei Sun at Oak Ridge National Laboratory for fruitful discussions. W.D.L. and F.W. acknowledge financial support from National Natural Science Foundation of China under Grants No. 51371195, No. 11675255, No. 11374197, and No. 11634008. O.E. acknowledges financial support from KAW (Projects No. 2013.0020 and No. 2012.0031). The calculations were performed at Supercomputer Centre in China Spallation Neutron Source.

[1] S. Heathman, R. G. Haire, T. Le Bihan, A. Lindbaum, M. Idiri, P. Normile, S. Li, R. Ahuja, B. Johansson, and G. H. Lander, Science **309**, 110 (2005).

[2] R. Atta-Fynn and A. K. Ray, Phys. Rev. B **76**, 115101 (2007).

[3] K. T. Moore and G. van der Laan, Rev. Mod. Phys. **81**, 235 (2009).

[4] I. D. Prodan, G. E. Scuseria, and R. L. Martin, Phys. Rev. B **73**, 045104 (2006).

[5] I. D. Prodan, G. E. Scuseria, and R. L. Martin, Phys. Rev. B **76**, 033101 (2007).

[6] L. Petit, A. Svane, Z. Szotek, W. M. Temmerman, and G. M. Stocks, Phys. Rev. B **81**, 045108 (2010).

[7] Q. Yin, A. Kutepov, K. Haule, G. Kotliar, S. Y. Savrasov, and W. E. Pickett, Phys. Rev. B **84**, 195111 (2011).

[8] X. D. Wen, R. L. Martin, G. E. Scuseria, S. P. Rudin, and E. R. Batista, J. Phys. Chem. C **117**, 13122 (2013).

[9] J. W. L. Pang, W. J. L. Buyers, A. Chernatynskiy, M. D. Lumsden, B. C. Larson, and S. R. Phillpot, Phys. Rev. Lett. **110**, 157401 (2013).

[10] T. Bo, J. H. Lan, Y. L. Zhao, Y. J. Zhang, C. H. He, Z. F. Chai, and W. Q. Shi, J. Nucl. Mater. **454**, 446 (2014).

[11] T. Bo, J. H. Lan, C. Z. Wang, Y. L. Zhao, C. H. He, Y. J. Zhang, Z. F. Chai, and W. Q. Shi, J. Phys. Chem. C **118**, 21935 (2014).

[12] J. W. L. Pang, A. Chernatynskiy, B. C. Larson, W. J. L. Buyers, D. L. Abernathy, K. J. McClellan, and S. R. Phillpot, Phys. Rev. B **89**, 115132 (2014).

[13] P. Seth, P. Hansmann, A. van Roekeghem, L. Vaugier, and S. Biermann, Phys. Rev. Lett. **119**, 056401 (2017).

[14] N. Lanatà, Y. X. Yao, X. Y. Deng, V. Dobrosavljević, and G. Kotliar, Phys. Rev. Lett. **118**, 126401 (2017).

[15] P. Maldonado, L. Paolasini, P. M. Oppeneer, T. R. Forrest, A. Prodi, N. Magnani, A. Bosak, G. H. Lander, and R. Caciuffo, Phys. Rev. B **93**, 144301 (2016).

[16] C. E. Boettger and A. K. Ray, Int. J. Quantum Chem. **90**, 1470 (2002).

[17] B. T. Wang, H. L. Shi, W. D. Li, and P. Zhang, Phys. Rev. B **81**, 045119 (2010).

[18] S. L. Dudarev, G. A. Botton, S. Y. Savrasov, C. J. Humphreys, and A. P. Sutton, Phys. Rev. B **57**, 1505 (1998).

[19] P. Zhang, B. T. Wang, and X. G. Zhao, Phys. Rev. B **82**, 144110 (2010).

[20] B. T. Wang, P. Zhang, R. Lizárraga, I. Di Marco, and O. Eriksson, Phys. Rev. B **88**, 104107 (2013).

[21] M. E. Manley, J. R. Jeffries, A. H. Said, C. A. Marianetti, H. Cynn, B. M. Leu, and M. A. Wall, Phys. Rev. B **85**, 132301 (2012).

[22] J. J. Zheng, B. T. Wang, I. Di Marco, and W. D. Li, Int. J. Hydrogen Energy **39**, 13255 (2014).

[23] M. Colarieti-Tosti, O. Eriksson, L. Nordstrom, J. M. Wills, and M. S. S. Brooks, Phys. Rev. B **65**, 195102 (2002).

[24] F. Zhou and V. Ozolins, Phys. Rev. B **83**, 085106 (2011).

[25] B. T. Wang, H. L. Shi, W. D. Li, and P. Zhang, J. Nucl. Mater. **399**, 181 (2010).

[26] Y. Lu, Y. Yang, F. W. Zheng, B. T. Wang, and P. Zhang, J. Nucl. Mater. **441**, 411 (2013).

[27] J. P. Dancausse, R. G. Haire, S. Heathman, and U. Benedict, J. Nucl. Sci. Technol. **3**, 136 (2002).

[28] R. J. M. Konings, J. Nucl. Mater. **298**, 255 (2001).

[29] P. Villars and L. D. Calvert, *Pearsons Handbook of Cystallographic Data for Intermetallic Phases*, 2nd ed. (ASM International, Ohio, 1991).
[30] L. R. Morss, J. W. Richardson, C. W. Williams, G. H. Lander, A. C. Lawson, N. M. Edelstein, and G. V. Shalimoff, J. Less-Common Met. **156**, 273 (1989).
[31] V. Sobolev, J. Nucl. Mater. **389**, 45 (2009).
[32] S. Li, R. Ahuja, and B. Johansson, High Press. Res. **22**, 471 (2002).
[33] F. Niikura and T. Hotta, Phys. Rev. B **83**, 172402 (2011).
[34] J. T. Pegg, X. Aparicio-Anglès, M. Storr, and N. H. de Leeuw, J. Nucl. Mater. **492**, 269 (2017).
[35] M. T. Suzuki, N. Magnani, and P. M. Oppeneer, Phys. Rev. B **88**, 195146 (2013).
[36] V. Milman, B. Winkler, and C. J. Pickard, J. Nucl. Mater. **322**, 165 (2003).
[37] A. Bouasria, A. Zaoui, S. Ait Abderrahmane, S. Kacimi, A. Boukortt, M. Bejar, and E. Dhahri, Int. J. Comp. Mat. Sci. Eng. **06**, 1750006 (2017).
[38] G. Kresse and J. Furthmüller, Phys. Rev. B **54**, 11169 (1996).
[39] W. Kohn and L. J. Sham, Phys. Rev. **140**, A1133 (1965).
[40] J. P. Perdew, K. Burke, and Y. Wang, Phys. Rev. B **54**, 16533 (1996).
[41] H. J. Monkhorst and J. D. Pack, Phys. Rev. B **13**, 5188 (1976).
[42] S. L. Dudarev, M. R. Castell, G. A. Botton, S. Y. Savrasov, C. Muggelberg, G. A. D. Briggs, A. P. Sutton, and D. T. Goddard, Micron **31**, 363 (2000).
[43] S. L. Dudarev, D. N. Manh, and A. P. Sutton, Philos. Mag. B **75**, 613 (1997).
[44] A. I. Liechtenstein, V. I. Anisimov, and J. Zaanen, Phys. Rev. B **52**, R5467 (1995).
[45] O. Eriksson, A. Bergman, L. Bergqvist, and J. Hellsvik, *Atomistic Spin Dynamics: Foundations and Applications* (Oxford University Press, Oxford, UK, 2017).
[46] F. Birch, Phys. Rev. **71**, 809 (1947).
[47] B. T. Wang, P. Zhang, H. Z. Song, H. L. Shi, D. F. Li, and W. D. Li, J. Nucl. Mater. **401**, 124 (2010).
[48] R. Hill, Phys. Phys. Soc. London **65**, 349 (1952).
[49] C. Cozzo, D. Staicu, J. Somers, A. Fernandez, and R. J. M. Konings, J. Nucl. Mater. **416**, 135 (2011).
[50] Y. Wang, L. Q. Chen, and Z. K. Liu, Comput. Phys. Commun. **185**, 2950 (2014).
[51] A. Siegel, K. Parlinski, and U. D. Wdowik, Phys. Rev. B **74**, 104116 (2006).
[52] P. Souvatzis, A. Delin, and O. Eriksson, Phys. Rev. B **73**, 054110 (2006).
[53] C. W. Greeff and M. J. Graf, Phys. Rev. B **69**, 054107 (2004).
[54] A. Sommerfeld and N. H. Frank, Rev. Mod. Phys. **3**, 1 (1931).
[55] Q. Yin and S. Y. Savrasov, Phys. Rev. Lett. **100**, 225504 (2008).
[56] G. A. Slack, J. Phys. Chem. Solids **34**, 321 (1973).
[57] G. A. Slack, Solid State Phys. **34**, 1 (1979).
[58] M. A. Blanco, E. Francisco, and V. Luaña, Comput. Phys. Commun. **158**, 57 (2004).
[59] J. R. Peterson and J. Fuger, J. Inorg. Nucl. Chem. **33**, 4111 (1971).
[60] B. C. Frazer, G. Shirane, D. E. Cox, and C. E. Olsen, Phys. Rev. **140**, A1448 (1965).
[61] A. Bendjedid, T. Seddik, R. Khenata, H. Baltache, G. Murtaza, A. Bouhemadou, S. Bin Omran, S. Azam, and S. A. Khan, J. Magn. Magn. Mater. **396**, 190 (2015).
[62] X. D. Wen, R. L. Martin, L. E. Roy, G. E. Scuseria, S. P. Rudin, E. R. Batista, T. M. McCleskey, B. L. Scott, E. Bauer, J. J. Joyce, and T. Durakiewicz, J. Chem. Phys. **137**, 154707 (2012).
[63] J. P. Dancausse, E. Gering, S. Heathman, and U. Benedict, High Press. Res. **2**, 381 (1990).
[64] M. Idiri, T. Le Bihan, S. Heathman, and J. Rebizant, Phys. Rev. B **70**, 014113 (2004).
[65] B. Dorado and P. Garcia, Phys. Rev. B **87**, 195139 (2013).
[66] Y. J. Zhang, B. T. Wang, Y. Lu, Y. Yang, and P. Zhang, J. Nucl. Mater. **430**, 137 (2012).
[67] I. D. Prodan, G. E. Scuseria, J. A. Sordo, K. N. Kudin, and R. L. Martin, J. Chem. Phys. **123**, 014703 (2005).
[68] Y. Baer and J. Schoenes, Solid State Commun. **33**, 885 (1980).
[69] T. M. McCleskey, E. Bauer, Q. X. Jia, A. K. Burrell, B. L. Scott, S. D. Conradson, A. Mueller, L. Roy, X. D. Wen, G. E. Scuseria, and R. L. Martin, J. Appl. Phys. **113**, 013515 (2013).
[70] C. Suzuki, T. Nishi, M. Nakada, M. Akabori, M. Hirata, and Y. Kaji, J. Phys. Chem. Solids **73**, 209 (2012).
[71] M. Sanati, R. C. Albers, T. Lookman, and A. Saxena, Phys. Rev. B **84**, 014116 (2011).
[72] J. F. Nye, *Physical Properties of Crystals* (Oxford University Press, Oxford, 1985).
[73] B. T. Wang, P. Zhang, H. L. Shi, B. Sun, and W. D. Li, Eur. Phys. J. B **74**, 303 (2010).
[74] M. Noé and J. R. Peterson, Inorg. Nucl. Chem. Let. **8**, 897 (1972).
[75] W. C. Mosley, J. Inorg. Nucl. Chem **34**, 539 (1972).
[76] C. Kittel, *Introduction to Solid State Physics*, 7th ed. (Wiley, New York, 1996).
[77] M. A. Mignanelli and R. Thetford, in *Workshop Proceedings Advanced Reactors with Innovative Fuels* (British Nuclear Fuels Limited, Chester, UK, 2001).
[78] B. T. Wang, J. J. Zheng, X. T. Qu, W. D. Li, and P. Zhang, J. Alloys Compd. **628**, 267 (2015).
[79] Y. Lu, Y. Yang, and P. Zhang, J. Phys.: Condens. Matter **24**, 225801 (2012).